metals

MDPI

Article

Effects of Pre-Weld Heat Treatment and Heat Input on Metallurgical and Mechanical Behaviour in HAZ of Multi-Pass Welded IN-939 Superalloy

Amirhossein Mashhuriazar [1], Hamid Omidvar [1,*], Zainuddin Sajuri [2,*], C. Hakan Gur [3] and Amir Hossein Baghdadi [2,*]

1 Department of Materials and Metallurgical Engineering, Amirkabir University of Technology, Tehran 1599637111, Iran; amir.ama@aut.ac.ir
2 Department of Mechanical and Manufacturing Engineering, Faculty of Engineering and Built Environment, Universitiy Kebangsaan Malaysia, Bangi 43600, Selangor, Malaysia
3 Department of Metallurgical and Materials Engineering, Middle East Technical University, Ankara 06800, Turkey; chgur@metu.edu.tr
* Correspondence: omidvar@aut.ac.ir (H.O.); zsajuri@ukm.edu.my (Z.S.); baghdadi.amirhossein@gmail.com (A.H.B.); Tel.: +98-(21)-6454-2978 (H.O.); +60-(3)-8911-8017 (Z.S.); +60-(3)-8911-8016 (A.H.B.)

Received: 19 September 2020; Accepted: 22 October 2020; Published: 30 October 2020



Abstract: Heat-affected zones (HAZs) of Inconel 939 (IN-939) superalloy are susceptible to cracking during welding process. Preventing cracking during the repair welding of turbine components is important. In this study, the effects of heat input and pre-welding heat treatment on the microstructure, mechanical properties and crack formation in tungsten inert gas welding of IN-939 were investigated. The whole specimens were welded using Inconel 625 filler in an Ar atmosphere and characterised by metallographic examinations and hardness measurements. Results showed that the microstructures of IN-939 HAZs were highly susceptible to cracking during welding due to increasing of γ' volume fraction. All of these cracks appeared in the HAZs and grew perpendicular to the melting zone along the grain boundaries. In this survey, the pre-welding heat treatment and heat input strongly affected the HAZ microstructure and hardness. However, the pre-welding heat treatment with 67% impact was more effective than heat input with 30% impact. Finally, hot tensile tests were carried out on the specimens of the base metal and the optimal specimens under similar operating conditions within 600 °C–800 °C. Welding process did not affect the yield strength of the superalloy but slightly decreased its ultimate strength and elongation by as much as 92% and 50%, respectively, of those of the base metal.

Keywords: Inconel superalloy; high-temperature alloy; welding; heat treatment; precipitation; mechanical properties

1. Introduction

Gas turbines are extensively used in aircraft propulsion, power generation and other industrial systems. In the past decades, the operating temperature of gas turbine engines has been increased to achieve high efficiency and performance of power generation. Therefore, most gas turbine components are exposed to extremely high temperatures and stresses [1,2]. High temperatures and huge centrifugal force gradually reduce the strength of the blades, thereby making them susceptible to damage and failure [3–6]. Ni-based superalloys, such as Inconel 939 (IN-939), are used for applications at high service temperatures under severe loading conditions for a very long period due to their excellent oxidation resistance and excellent creep performance. These superalloys are mostly applied for

components used in hot sections of gas turbines [4]. IN-939 has been considered as the most significant precipitation-strengthened Ni–Cr–Co superalloys and is extensively utilised in generating hot parts of gas turbines, such as blades and vanes; this alloy can also be extended through an alteration in Waspaloy. However, under extremely harsh operating conditions, turbine components degrade through various damage mechanisms, leading to crack and airfoil tip loss. A damaged blade can cause extensive harm to adjacent turbine rows and lead to interruption of the entire system. Turbine blade failures are among the main reasons for shutdown in power plants [7]. The demand for low-cost refurbishment of devastated turbine airfoils increases because the replacement of these parts is very expensive [8]. The cost of refurbishment can be reduced by repair welding instead of replacing damaged turbine components with new ones. Despite critical restrictions of Ni-based superalloys, fusion welding is the most promising and practical method to repair these superalloys [9]. However, precipitation-strengthened Ni-based superalloys, such as IN-939, are incredibly susceptible to microfissuring in heat-affected zones (HAZs) during welding; the weldability of this alloy is poor due to abstained amounts of γ' formers, such as Al and Ti [10–13]. Xie et al. [14] reported that two kinds of crack, namely, liquation cracking and strain age cracking, commonly occur in the HAZ of the welded precipitation-hardened nickel-base superalloys.

Several studies were conducted on IN-939 and other similar superalloys to understand the cracking behaviour at the HAZ of welds. Bidron et al. [15] carried out induction pre-heating to reduce the hot cracking sensitivity of CM-247LC superalloy. They reported that pre-heating with the highest temperatures can help prevent hot cracking due to the dissolution of large γ' precipitates. Sidhu et al. [16] investigated the laser welding of Inconel 738. The result showed that using a directionally solidified version of the alloy can reduce the sensitivity of HAZ liquation cracking in Inconel 738. They claimed that HAZ cracking occurs in continuous cast alloy more than that in directionally solidified alloy. Sajuri et al. [17] found that primary cracks in the stationary blade of gas turbines were caused by improper welding repair of Inconel 738 and propagated in transgranular mode. Furthermore, Ye et al. [18] reported that in a multi-layer and multi-pass repair welding process of Inconel 718 superalloy, the hot cracking sensitivity significantly increased due to the longitudinal macro-segregation of craters and the transverse macro-segregation of welding centre in pre-layers.

Ola et al. [19] reported that the propensity for HAZ cracking depends on the compound of the filler alloy utilised during welding; those with less Al + Ti + Nb + Ta concentration were perceived to be less susceptible to cracking. Tajally [20] reported filler metals affected on HAZ cracking as the filler metals with lower concentrations of (Al + Ti + Nb + Ta + Mo + W) than the base metal can efficiently lessen the cracking.

González et al. [21] reported that the final microstructure of HAZ and the weldability of IN-939 can be affected by pre-weld heat treatment. The initial microstructure of the base metal (BM) directly affects the ultimate microstructure in the HAZ and has a significant impact on the morphology and volume fraction of γ' precipitates. Specimens with primary and secondary spherical γ' precipitates in their microstructure experienced less cracking in HAZ compared with those with square γ' precipitates. Furthermore, González et al. [22] investigated the influence of pre-weld heat treatment on the lattice parameters and determined the degree of mismatch between the crystalline lattice of γ' precipitates and γ substrate. They reported that a lower mismatch between γ' precipitates and substrate resulted in lower dislocation, density and lower local strain, leading to a significant reduction in crack formation.

Despite the importance and widespread use of welding for manufacturing and repair of components made of IN-939, few reports are available regarding the effects on welding metallurgy and weldability by adjusting welding parameters. The impact of each welding parameter on the size of cracks and determination of mechanical properties under operating conditions have not been reported yet. This study aims to examine the effect of repair welding parameters (i.e., pre-weld heat treatment and welding heat input) on microstructural changes obtained in IN-939 and the occurrence and size of cracks. The mechanical properties of the repaired weld under the optimal condition were compared with base metal at the operating temperature.

2. Materials and Methods

Specimens (120 mm × 50 mm × 10 mm) were prepared from the root of scrapped and damaged gas turbine (Siemens Energy, Munich, Germany) blades made of IN-939. The chemical composition of IN-939 is listed in Table 1. This Ni-base superalloy contains Co and Cr as the primary alloying elements, with Al and Ti contents of 1.59% and 3.22%, respectively. Welding was performed using gas tungsten arc welding (GTAW) method in an argon atmosphere with Inconel 625 filler [19], at a voltage of 10 V and a linear speed of 75 mm/min in four side-by-side passes (Figure 1).

Table 1. Chemical composition of the base metal and filler metal (wt%).

Material Grade	Ni	Al	Ti	Mn	B	Nb	Mo	Ta	C	W	Co	Cr
IN-939	Balance	1.59	3.22	0.02	0.01	0.65	0.24	2.00	0.14	2.53	16.08	27.1
IN-625	Balance	0.40	0.40	0.50	-	3.15	10.00	-	1.00	-	1.00	20.00

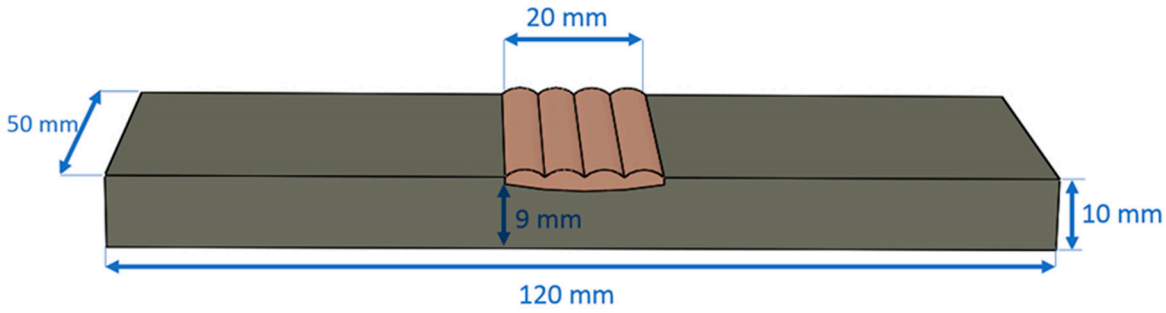


Figure 1. Schematic of the welded specimen in four side-by-side welding passes.

The experiments were divided into two groups to investigate the effect of pre-weld heat treatment and welding heat input. The heat input energy (kJ/mm) of the arc can be calculated by the method of González et al. [22]:

$$\text{Heat input} = (V \times A \times 60)/(S \times 1000) \quad (1)$$

where V, A and S are arc voltage, welding current and arc travel speed, respectively.

Pre-weld heat treatment strongly affects the cracking of HAZ. According to recent studies, four different heat treatment cycles were selected to survey the influence of pre-weld heat treatment on HAZ cracking. The succession of the four various heat treatments applied to the samples is as follows: (A) solution heat treatment for 4 h according to the study of Tajally [23], (B) 10 h heat treatment recommended by González et al. [21], (C) 14 h heat treatment recommended by Shaw and Smith [24] and (D) 50 h heat treatment originally recommended for IN-939 by Delargy [25]. Pre-weld heat treatment was performed in a vacuum furnace under 10^{-5} Torr pressure. The specifications of the heat treatment and applied heat input are provided in Table 2, and the heat treatment sequences are illustrated in Figure 2.

Table 2. List of heat treatments applied to the specimens.

No.	Specimen Name	Heat Treatment	Current (A)	Heat Input (kJ/mm)
1	A1	1160 °C/4 h	60	0.45
2	A2	1160 °C/4 h	70	0.45
3	B1	1160 °C/4 h + 1000 °C/6 h	60	0.45
4	B2	1160 °C/4 h + 1000 °C/6 h	70	0.60
5	C1	1160 °C/4 h + 1000 °C/6 h + 800 °C/4 h	60	0.45
6	C2	1160 °C/4 h + 1000 °C/6 h + 800 °C/4 h	70	0.60
7	D1	1160 °C/4 h + 1000 °C/6 h + 900 °C/24 h + 700 °C/16 h	60	0.45
8	D2	1160 °C/4 h + 1000 °C/6 h + 900 °C/24 h + 700 °C/16 h	70	0.60

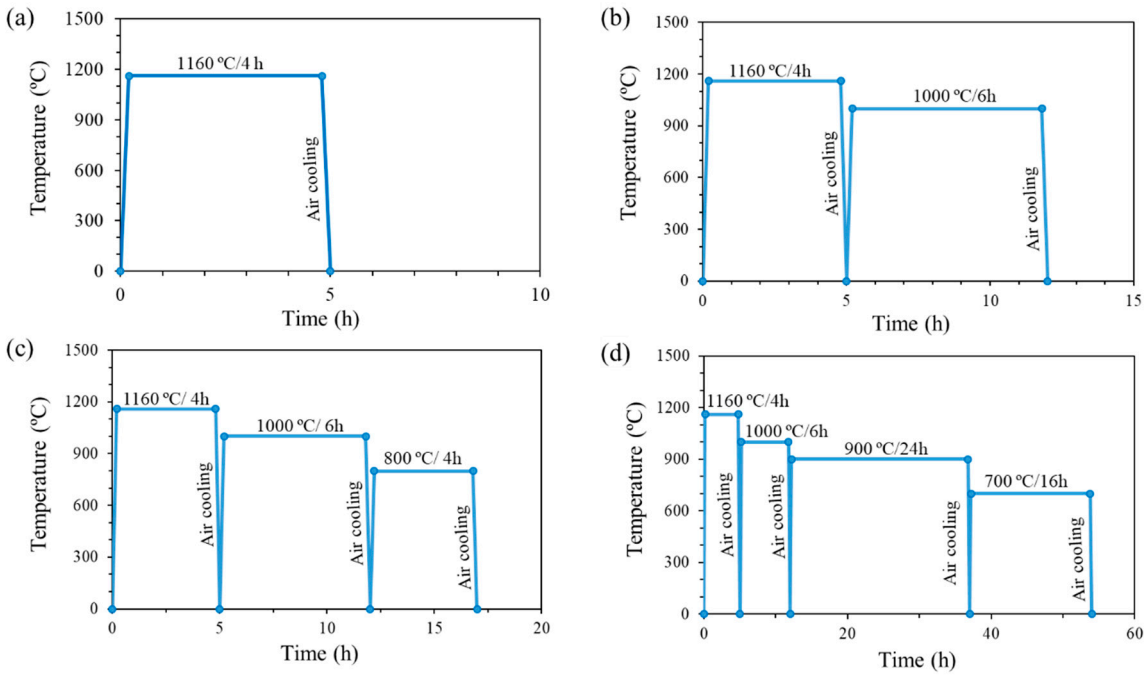


Figure 2. Applied heat treatment process; (**a**) process A, (**b**) process B, (**c**) process C and (**d**) process D.

The microfissuring susceptibility of HAZ depends on the composition and microstructure of the material. Therefore, phase changes were simulated using JMatPro® V7 software (V7, Sente software Ltd., Surrey, UK). Microstructure and phases were examined using an optical microscope (Olympus Optical Co., Ltd., Shinjuku-ku, Japan) and a field emission scanning electron microscope (FESEM) (FESEM MIRA3 XMU TESCAN, Kohoutovice, Czech Republic). The chemical composition at different zones of weldments was determined using energy-dispersive X-ray spectroscopy (EDS) (Carl Zeiss Microscopy GmbH, Jena, Germany) analysis. The microhardness of the welded samples was also measured using a Vickers hardness tester (ZwickRoell, Ulm, Germany) with applied force of 9.8 N and a dwell time of 15 s according to ASTM E92. Image J 1.44p® software (NIH Image, Bethesda, MD, USA) was applied to measure the average size of different welding zones, the area fraction of precipitation phases and the length of cracks for five cross-sections of the samples [26]. Tensile test was performed on the samples by using a universal testing machine (ZwickRoell, Ulm, Germany) of 600 °C, 700 °C and 800 °C to compare the mechanical properties of the base metal (BM) with those of the welded specimen that was identified by optimum mechanical properties.

3. Results and Discussion

3.1. Phase Equilibrium Diagram

JMatPro® software was used to simulate phase distribution in terms of temperature based on the chemical composition of BM for a better understanding of the transformations that occurred during various stages of heat treatment (Table 1) [27]. According to the phase simulation results, approximately all the precipitation phases that have nucleation in the solidification phase (Figure 3), except for MC carbides, dissolved in the austenitic gamma matrix at 1160 °C. The gamma-prime phase, which is the essential strengthening phase of IN-939, disappeared at approximately 1100 °C [24].

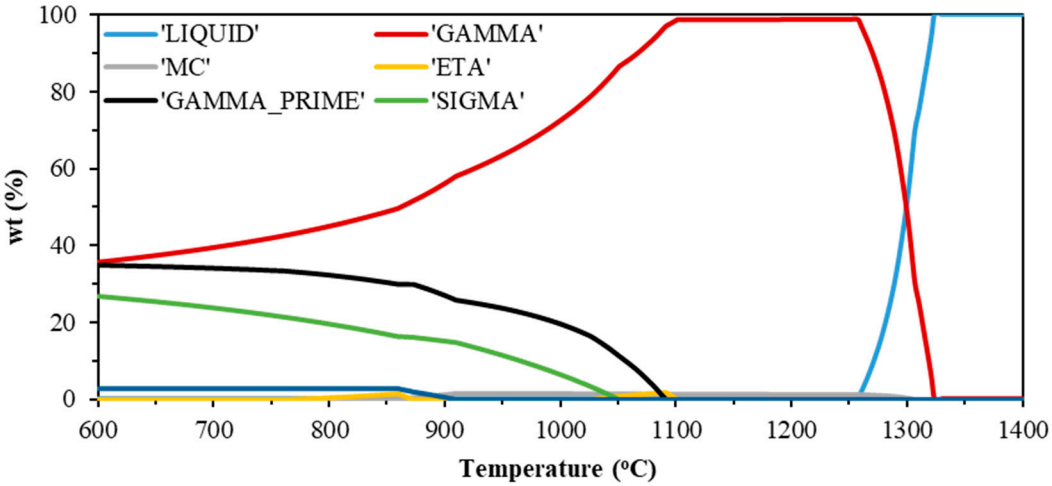


Figure 3. Phase equilibrium diagram of IN-939 obtained from JMatPro® simulation software.

Figure 4 shows the changes in the chemical composition of carbides with temperature. In Figure 4a, $M_{23}C_6$ carbide was rich in Cr but contained smaller amounts of Mo and W. These carbides are essential determinants of the mechanical properties of superalloys. According to a study performed by Hu et al. [28], $M_{23}C_6$ carbide precipitation behaviour was influenced obviously by grain boundary characteristic and interfacial energy. These carbides precipitated only at the large-angle grain boundaries with high interfacial energy. Considering the coherent orientation relationship between $M_{23}C_6$ and the matrix, $M_{23}C_6$ carbides can be precipitated with four typical morphologies that have a significant impact on mechanical properties.

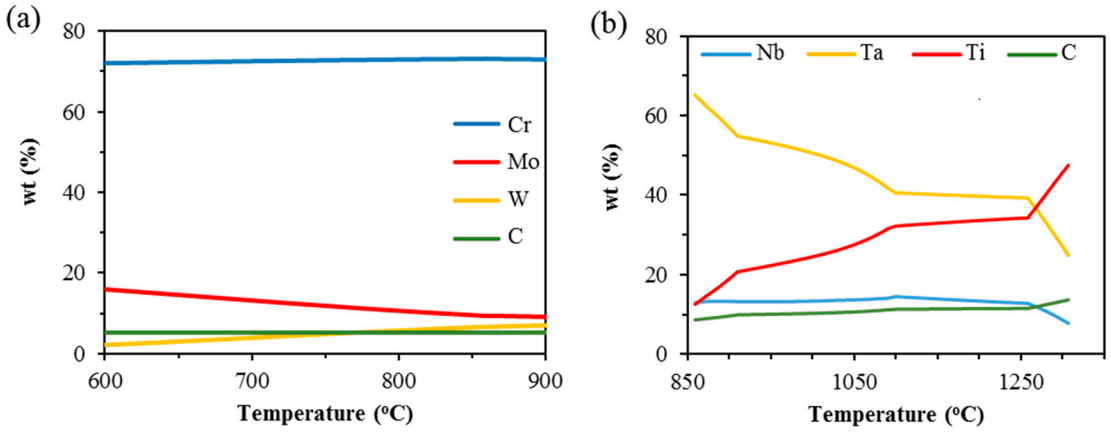


Figure 4. Changes in the chemical composition of carbides at different temperatures: (**a**) $M_{23}C_6$ and (**b**) MC.

Figure 4b shows the changes in the chemical composition of MC carbides with temperature. These carbides were rich in Ta, Ti and Nb and more stable at higher temperatures (734 °C–1267 °C) than $M_{23}C_6$ carbide (below 734 °C). The chemical composition of MC carbide was almost constant. However, Ti content slightly increased with temperature, and the Ta content slightly decreased due to the dissolution of gamma-prime precipitates at temperatures above 1090 °C [29].

Figure 5 shows the changes in the elemental composition of primary precipitates in IN-939 at different temperatures. At temperatures between 900 °C and 850 °C, the MC carbide entered a reaction with the gamma matrix. Jahangiri et al. [30] claimed that MC carbides transformed into $M_{23}C_6$ carbides and γ′ phases at high temperatures or into η phase at low temperatures.

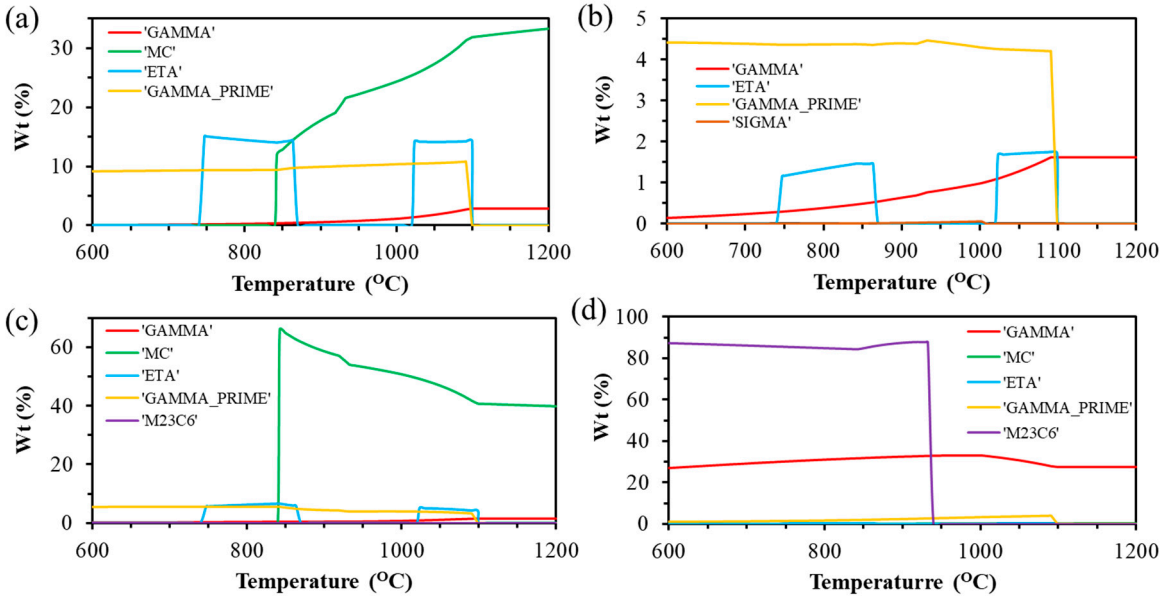


Figure 5. Changes in precipitation phases in IN-939 with temperature; (**a**) Ti, (**b**) Al, (**c**) Ta and (**d**) Cr.

3.2. Microstructural Examination

3.2.1. Base Metal Microstructure

Figure 6a shows the microstructure of the base metal of the as-cast IN-939 with dendrite morphology. The high-magnification image of the base metal is presented in Figure 6b,c. Various MC carbide phases precipitated at the grain boundaries or within the grains, where M is predominated by Ti [31]. The role of carbides is significant in Ni-based superalloys because they improve the tensile properties and rupture strength via uniform distribution and dispersion [32,33]. Jahangiri et al. [26] reported the formation of $M_{23}C_6$ and η during the decomposition of MC carbides at temperatures below 800 °C according to Equation (2), which is reported by Lvov et al. [34];

$$MC + \gamma/\gamma' \rightarrow M_{23}C_6 + \eta \quad (2)$$

Changes in the chemical composition of primary precipitates at different temperatures are shown in Figure 5. η phase can be generated during the decomposition of MC carbides at low temperatures. During the decomposition of MC, carbon diffuses outside the carbide into the γ-matrix, thereby forming Cr-rich ($M_{23}C_6$) carbides at the MC-γ/γ′ interface and hexagonal η [Ni_3(Ti, Ta)] phase [35]. Yan et al. [36] stated that MC carbides were transformed into Cr-rich carbides and γ′ phases at temperatures higher than 850 °C in accordance with Equation (3);

$$MC + \gamma \rightarrow M_{23}C_6 + \gamma' \quad (3)$$

At temperatures higher than 850 °C, no η phase was found in the transformed areas near the MC carbides. Under both conditions (i.e., below 800 °C and above 850 °C), $M_{23}C_6$ carbides were generated. However, the morphology of $M_{23}C_6$ carbides can be affected by temperature. Bai et al. [37] claimed that these carbides displayed lamellar morphology at the grain boundaries at low temperatures.

Table 3 illustrates the results of EDS analysis performed on Points A and B in the BM [Figure 6c]. On the basis of the EDS quantitative investigation, the composition of point A was characterised as MC carbide (Ti = 47.04 wt%, Ta = 28.68 wt%, Nb = 25.24 wt%), and point B was identified as η phase (Ni = 50.93 wt%, Ti = 27.05 wt%). Figure 6d shows the γ′ precipitates, [(Ni, Co)$_3$(Al, Ti, Nb)], which were observed in L12 ordered intermetallics. This precipitate plays the main role in strengthening the material at high temperatures.

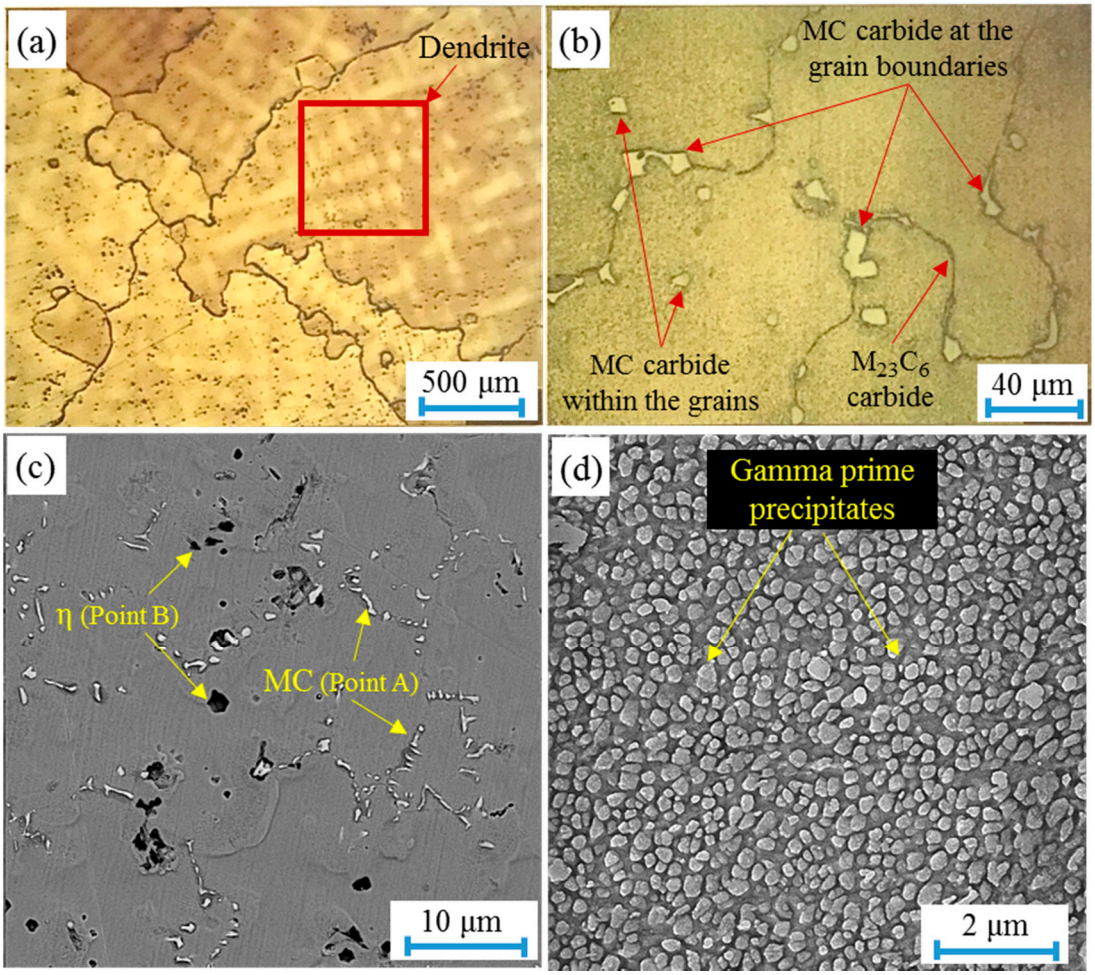


Figure 6. Microstructure of the BM under casting conditions; (**a**) dendrite morphology of the as-cast BM, (**b**) MC carbide precipitated at the grain boundaries, (**c**) MC and η phases and (**d**) γ´ precipitates.

Table 3. Chemical analysis (wt. %) illustrated in Figure 5c.

Location Point	Ni	Ti	Nb	Ta	Co	Cr	Phase
Point A	2.06	47.04	25.24	28.68	0.45	0.24	MC
Point B	50.93	27.05	5.89	6.02	2.49	5.06	η

3.2.2. Pre-Weld Heat Treatment Effect on the Microstructure

Figure 7 shows the effect of different pre-weld heat treatments on the microstructure of BM. Figure 7a shows the microstructure of specimen A that was subjected to solution heat treatment at 1160 °C for 4 h. This treatment takes all the γ′ and practically η precipitates into the solution and achieves homogenisation [38]. The microstructure contained a γ′ phase with irregular morphology, a diameter of approximately 252 nm and a volume fraction of about 32% in the austenitic gamma matrix. The microstructure of specimen B is illustrated in Figure 7b. This specimen was subjected to solution heat treatment followed by aging at 1000 °C for 6 h. The aging treatment changed the irregular morphology of γ′ into spherical morphology with an average diameter of approximately 258 nm and a volume fraction of about 39%.

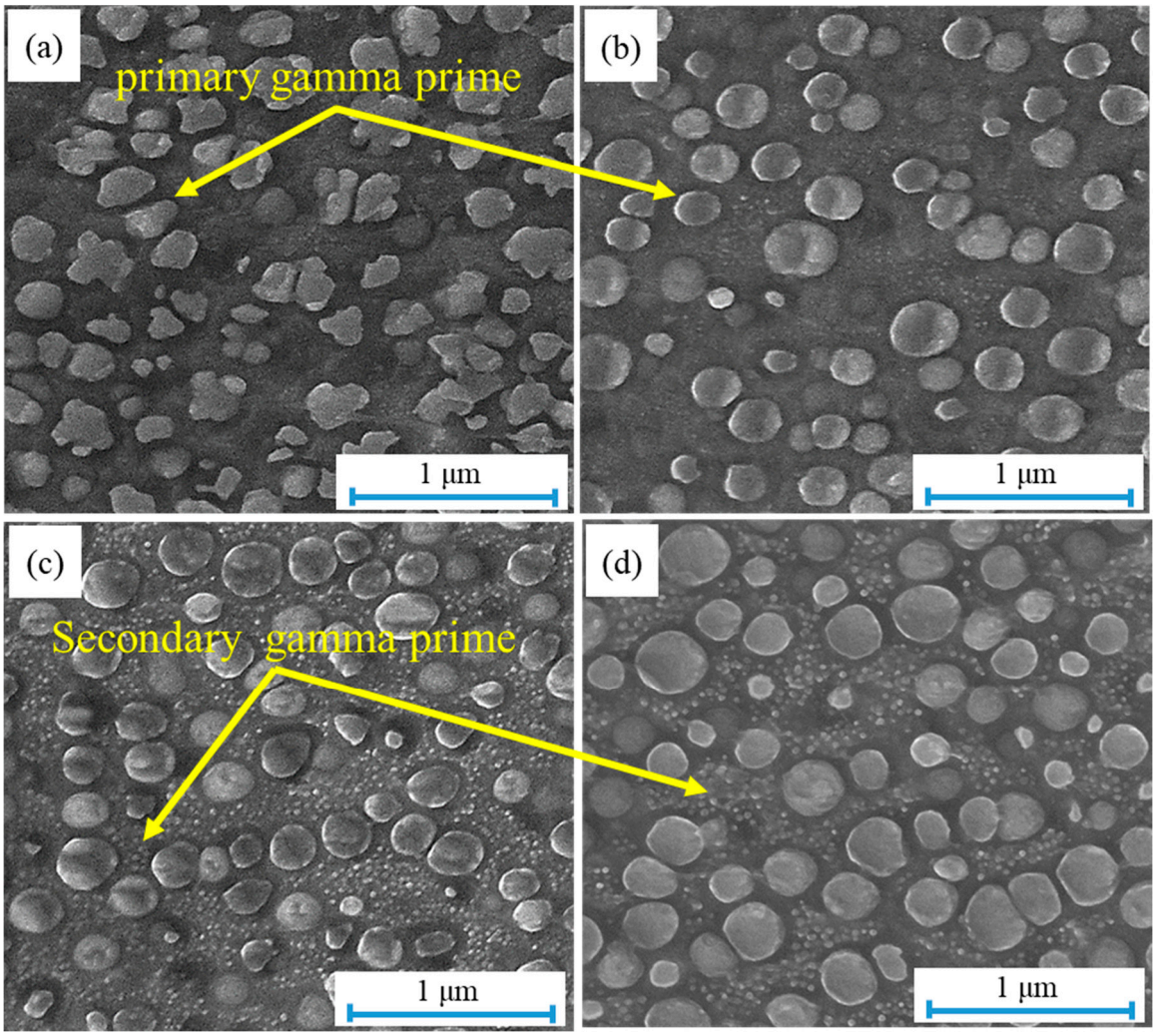


Figure 7. Effect of different pre-welding heat treatments on the microstructure of BM; (**a**) specimen A, (**b**) specimen B, (**c**) specimen C and (**d**) specimen D.

Figure 7c displays the microstructure of specimen C that was subjected to solution heat treatment followed by two stages of aging, namely, primary aging at 1000 °C for 6 h and secondary aging at 800 °C for 4 h. The microstructure analysis revealed primary and secondary γ′ precipitates with diameters of approximately 250 and 35 nm, respectively, with a volume fraction of 45% due to secondary aging treatment. The microstructure of specimen D is shown in Figure 7d. This specimen was subjected to solution heat treatment followed by primary and secondary aging at 700 °C for 16 h. The microstructure also contained primary and secondary spherical γ′ precipitates, and the average grain diameter increased and reached 266 and 33 nm for primary and secondary γ′, respectively.

3.2.3. Welded Specimen Microstructure

Figure 8 shows the effect of the welding process on γ′ precipitate distribution in the microstructure of the welded specimens in HAZ. Based on the micrograph, the precipitates maintain their original morphology, and a clear reduction in quantity and size of the precipitates were observed in all of the welded specimens comparing to those in BM (Figure 7) after the welding process. Comparisons of the size and volume fraction of γ′ precipitates between the BM and the HAZ are provided in detail as shown in Table 4. This behaviour (reduction in size and quantity) is attributed to the heat-activated dissolution. Furthermore, the initial particle size, morphology and heating rate affect the integrated time required for homogenization [39,40]. Also, increasing the heating rate and the particle precipitate

size are caused to shift the dissolution beginning toward the higher temperatures, but above the related dissolution temperature, dissolution occurs rapidly. However, during the non-equilibrium heating process like the welding cycle, the dissolution behaviour of γ′ particles will be changed. At this condition, the dissolution temperature of γ′ particles will be higher than their equilibrium dissolution temperature, and when the composition of the interface between precipitate particles and diffusion zone reaches the maximum solid solubility where the eutectic reaction occurs [22].

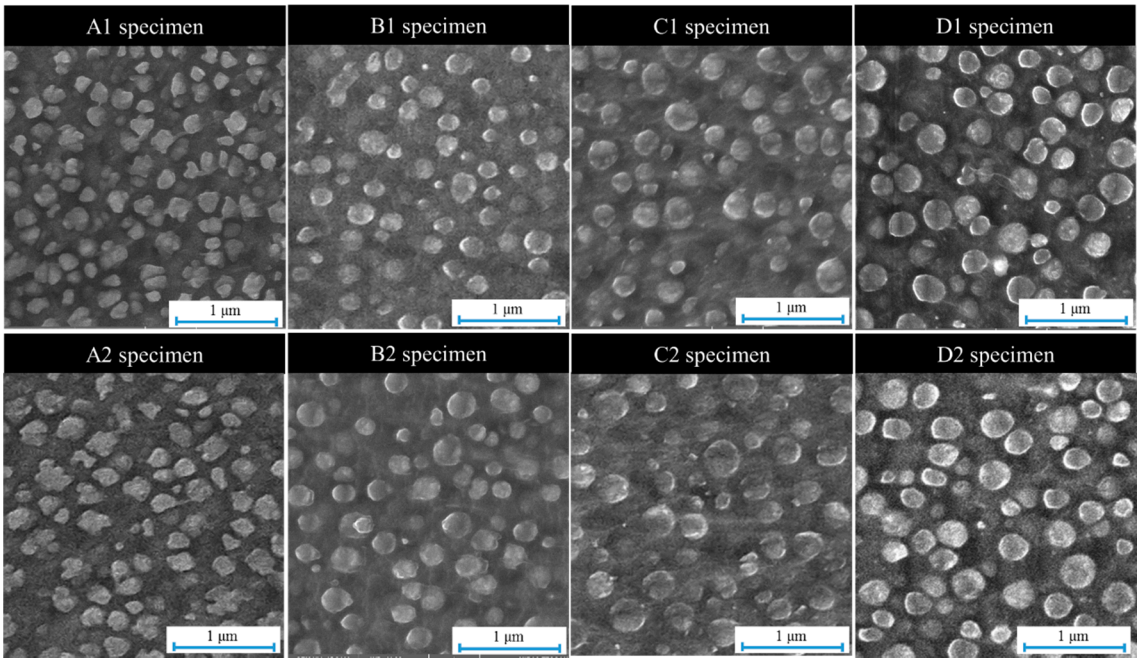


Figure 8. Effect of welding process on γ′ precipitate distribution in heat-affected zone microstructure of welded specimens.

Table 4. Comparison of the size and volume fraction of γ′ precipitates in the BM and the heat-affected zone of welded samples.

Sample Name		γ′ Phase Fraction (%)	γ′ Particle Sizes (nm)	
			Primary	Secondary
Base Metal	A	32.4	220	-
	B	38.6	248	-
	C	45.2	250	35
	D	49.4	266	36
Heat-Affected Zone	A1	27.7	238	-
	A2	28.8	249	-
	B1	32.6	254	-
	B2	34.3	270	-
	C1	33.1	268	-
	C2	34.8	277	-
	D1	37.8	278	-
	D2	49.1	294	-

Figure 9a shows the macrostructure of the cross-sectional view of the A1welded sample in different welding zones with the lowest γ′ volume fraction and size. For all of the samples, the cross-section morphology can be differentiated into three regions, namely, fusion zone (FZ), HAZ and BM. Figure 9b demonstrates the microstructure of the HAZ. The microstructure of the HAZ was influenced by many factors, such as the peak temperature of thermal cycling, heating rate, staying time at high temperature and subsequent cooling speed in accordance with the claim of Yan et al. [41]. Figure 9c shows the

columnar dendrites in the microstructure of FZ. The formation of these dendrites was due to the substrate acting as a heat sink; the temperature gradient at the bottom of the molten pool was higher than that in the other regions. Therefore, dendrites grew almost along the direction of the temperature gradient. Figure 9d shows the microstructure of the BM. Some coarse dendrites were found according to the microstructural stability of IN-939 [26]. In the dendritic microstructure, Ti, Nb, Ta and Zr segregated into the interdendritic regions, while Cr segregated to the dendrite cores.

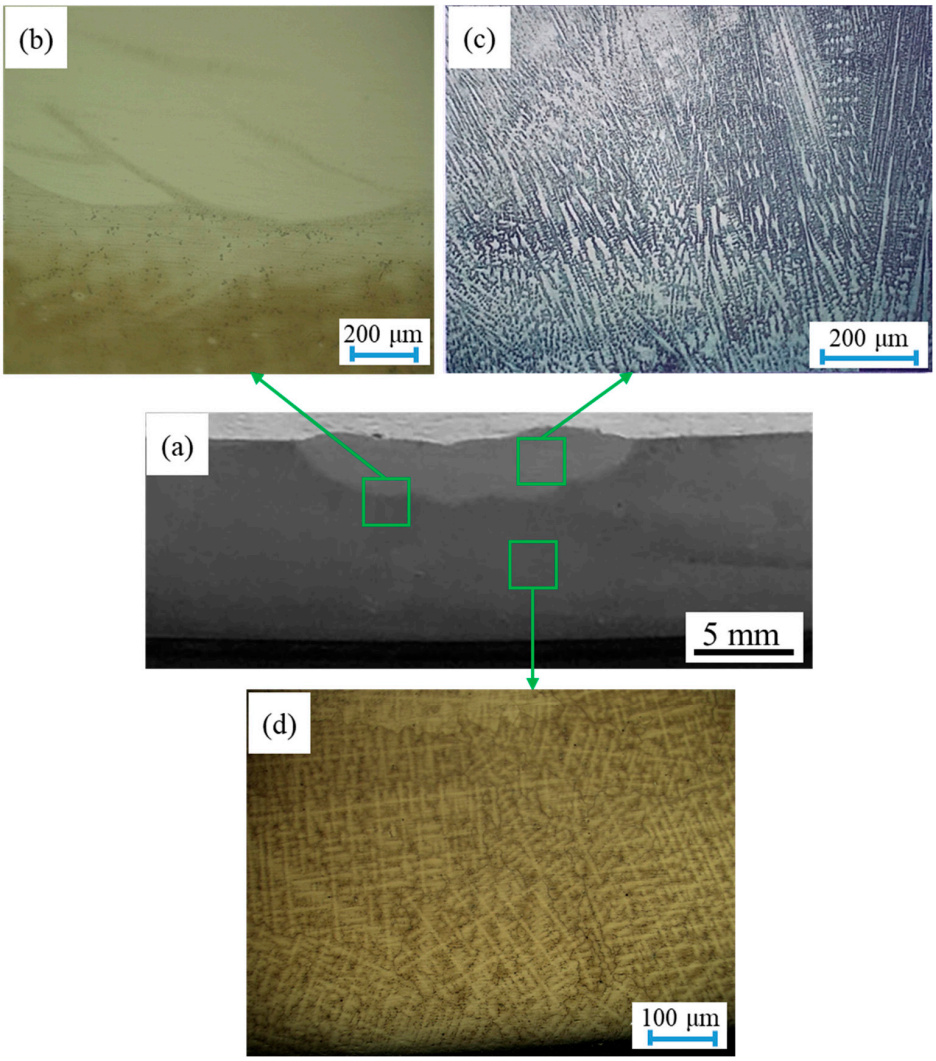


Figure 9. Microstructure of A1 welded specimen; (**a**) cross-section view, (**b**) HAZ, (**c**) FZ and (**d**) BM.

Figure 10a shows the microstructures of the three zones obtained in the A1 welded specimen as the result of welding. The microstructures of precipitation-hardened IN-939 were highly susceptible to crack at HAZ during the welding process [16]. A liquation crack of more than 400 µm in size originated from the HAZ. HAZ cracking in superalloys is attributable to intergranular liquation, caused by nonequilibrium melting of various phases, and the influence of on-cooling tensile stresses that cause de-cohesion along the liquated grain boundaries. Moreover, M23C6 and MC carbides were found near the crack zone in higher magnification and distributed in the HAZ [Figure 10b]. These cracks appeared in the HAZ and propagated intergranular perpendicular to the base metal along the grain boundaries. Similar observations about the weldability of IN-939 superalloy and HAZ's microstructure were reported in recent research [22]. Figure 10c presents the microstructure of the D1 welded specimen. The crack obtained in the D1 specimen was longer than that in the A1 specimen because of the higher volume fraction of γ' (Table 4) in the sample.

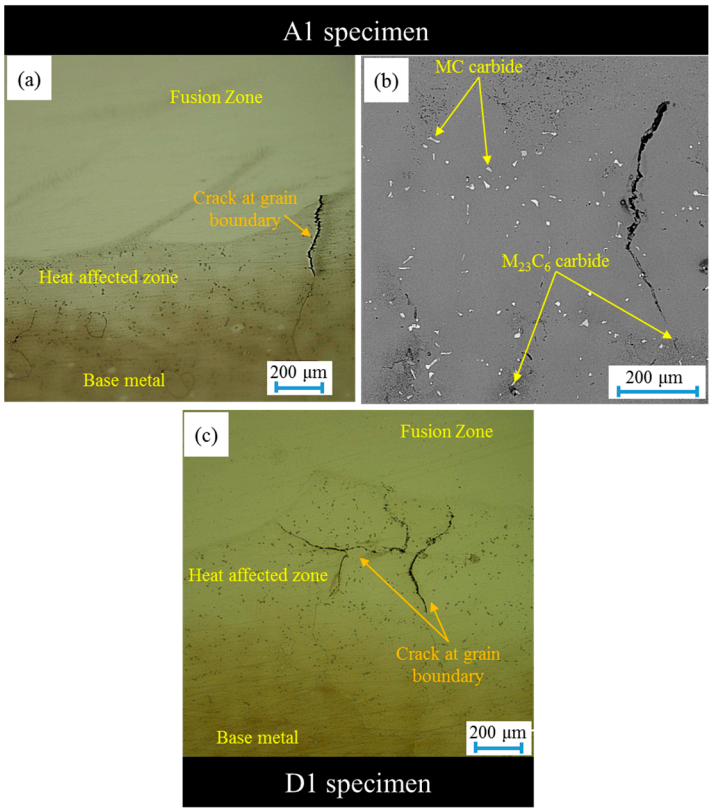


Figure 10. Cross-section view of the welded specimen; (**a**) different welding zones as the result of welding in A1 sample, (**b**) higher magnification of intergranular liquation crack and carbides in HAZ of A1 sample and (**c**) intergranular liquation crack formed in the HAZ of D1 sample.

Figure 11 shows the result of the EDS line analysis performed in the welding zone of the A1 specimen to identify changes in the chemical composition near the obtained crack. The HAZ had lower Al and Ti contents and higher Ni content than the BM, indicating a decrease in the amount of γ′ precipitates in the HAZ [24]. Furthermore, a good agreement was found between the EDS line scanning near the crack (Figure 11) and the results of the γ′ phase fraction in Table 4, where the volume fraction of γ′ was decreased from 32.4% (in sample A as base material) to 27.7% and 28.8% in welded samples of A1 and A2, respectively.

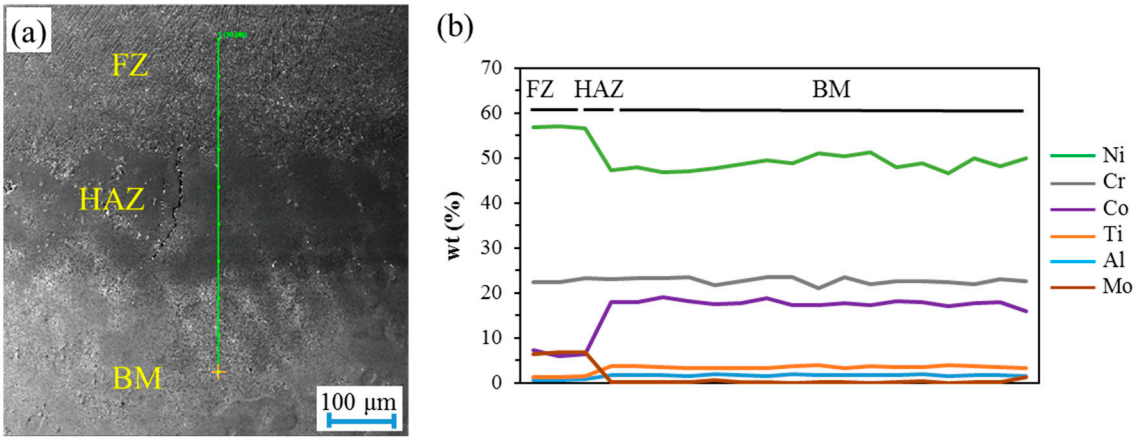


Figure 11. EDS line analysis of A1 welded specimen in the welding zone; (**a**) SEM photo and (**b**) changes in the chemical composition in the three welding zones.

Figure 12a displays the crack and re-melted layer at the grain boundaries. This crack was initiated from the boundary between the weld metal and the HAZ and propagated into the BM. Moreover, re-melting zones were found in the vicinity of the cracks. The cause of the crack nucleation seemed to be the melted layer. Yan et al. [41] specified that the HAZ liquation cracking can be developed through three steps, namely, intergranular liquation, crack initiation and propagation.

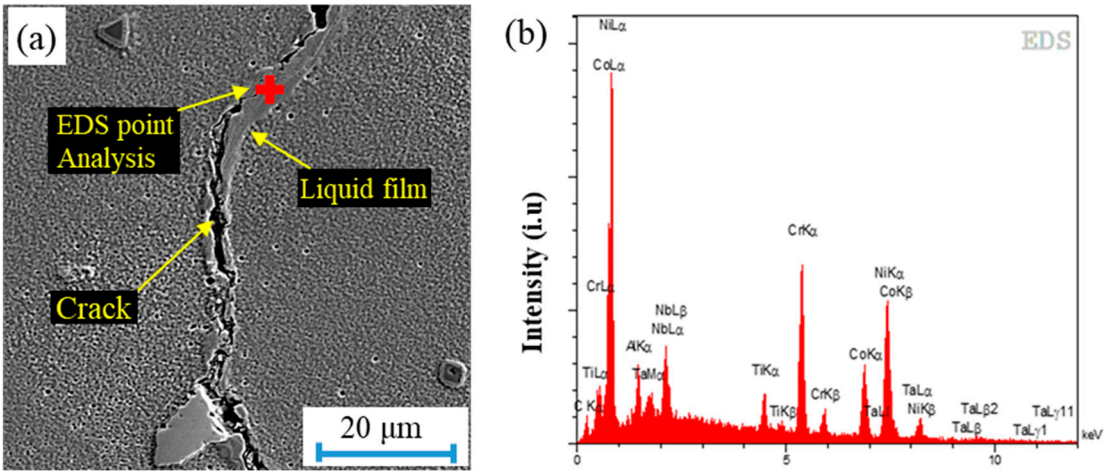


Figure 12. Elemental analysis of crack nucleation site: (**a**) SEM photo of liquid film and crack in the grain boundary and (**b**) EDS analysis of the liquid film.

The EDS point analysis performed near the crack at the liquid film [Figure 12b] emphasised the presence of MC and $M_{23}C_6$ carbides, including Nb, Ti and Cr, in the crack propagation site. This finding clarified the traces of other elements, such as Ni and Co, which are entirely reasonable for the evidence of adjacent elements to appear in the EDS analysis.

Li et al. [42] reported the manner of the M23C6 phase during the non-equilibrium heating process of welding. According to their results, lots of solute atoms released from particles diffuse into the adjacent matrix and create a diffusion zone with a great composition gradient. When the composition of the interface between particles and the diffusion zone reaches the maximum solid solubility and the temperature reaches the eutectic point the eutectic reaction occurs and liquation volume expands accordingly around the particles. And in the cooling condition, first, the γ phase precipitate from the liquid with a hypoeutectic composition. Then eutectic reaction occurs during the cooling condition and M23C6 and γ phase will precipitate from the remaining liquid. Further, in multi-layer welding when the matrix region was heated by subsequent welds due to the tempering effect, secondary M23C6 precipitated from the matrix. So, the manner of the micro-sized M23C6 in multi-layer welding cycle could be explained using the following equation:

$$M_{23}C_6 + (\gamma\text{-Ni}) \rightarrow \text{liquid} \rightarrow M_{23}C_6 + (\gamma\text{-Ni}) \rightarrow M_{23}C_6 + (\gamma\text{-Ni}) + \text{secondary } M_{23}C_6 \quad (4)$$

The cracking in the HAZ directly resulted from the reaction between intergranular liquation and mechanical driving force because of tensile stresses created during welding [14]. Therefore, Equation (5) defined the stress needed (σ) to prevail the surface tension at the grain boundary containing liquid film:

$$\sigma = 2\gamma_{SL}/h \quad (5)$$

where γ_{SL} and h are the surface tension and thickness of the liquid film, respectively. A low-hardening base alloy, such as IN-939, has the potential to relieve substantial stresses, thereby decreasing the moving force of intergranular liquation cracking. Thus, the resistance to cracking will increase by reducing the hardness in the HAZ. Therefore, hardness was measured at the weld cross-section.

3.3. Mechanical Properties

3.3.1. Tensile Strength

Figure 13 shows the tensile strength of the A1 welded samples at HAZ and the BM at temperatures of 600 °C, 700 °C and 800 °C. This diagram indicated that the welding process had a significant effect on the hot tensile properties of IN-939. The yield strength decreased from 674 MPa to 550 MPa in the BM and from 728 MPa to 538 MPa in the A1 welded specimen with increasing temperature from 600 °C to 800 °C. Moreover, the elongation value reduced as the temperature increased from 600 °C to 700 °C, but the opposite trend was observed when the temperature was increased from 700 °C to 800 °C in BM and A1 welded samples. This behaviour can be attributed to mechanical properties including the tensile behaviour of nickel, which is affected by the characteristics of the sedimentary phase of the gamma prime phase. In alloys with a high percentage of gamma prime phases, such as IN-939, the change in the phase characteristics will be a noticeable effect on the tensile strength [43]. Sajjadi et al. [44] reported that the tensile behaviour of superalloy is affected by the presence of γ′ precipitates and matrix. Not only γ′ precipitates but also the matrix plays a decisive role in alloy tensile behaviour. The γ phase also shows an increasing trend up to the temperature of 700 °C and an opposite trend at higher temperatures.

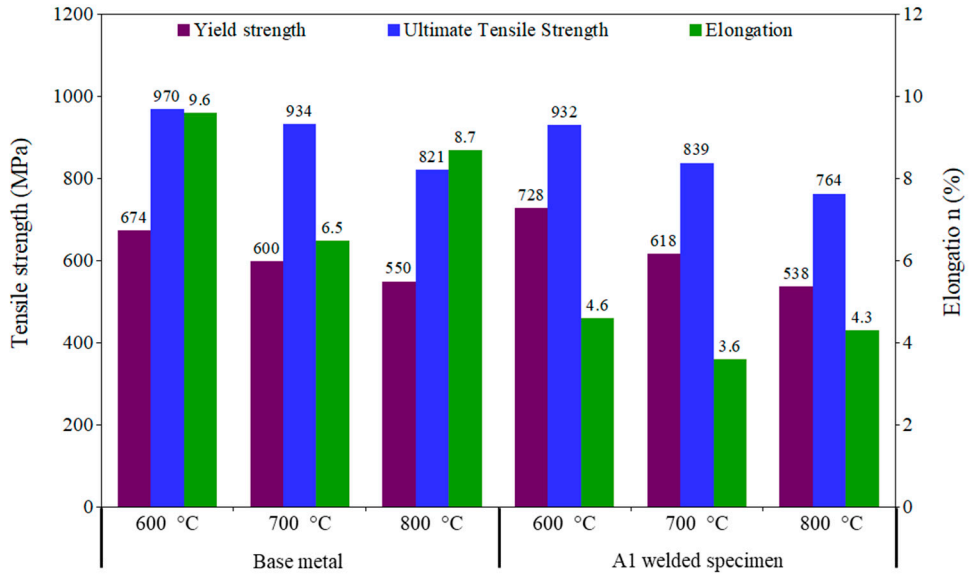


Figure 13. Tensile strength of BM and the HAZ of A1 welded samples at different temperatures.

Main factors such as size, volume fraction and distribution of γ′ precipitates influence the mechanical properties of precipitation-hardened nickel-based superalloy [45,46]. As mentioned in Figure 8, welding increased the size of γ′ precipitates for a similar volume fraction, which extended the inter-precipitate distance and diminished the stress needed to a displacement of dislocations to bow around precipitates [45].

Fractography analysis was conducted to specify the mode of failure after the tensile test (Figure 14). Figure 14a shows the fracture surface of the BM. The fracture surface consisted of cleavage facets and dimples, which are mostly known as a quasi-brittle fracture. Figure 14b shows the fracture surface of the A1 welded sample, which had cracks on the fracture surface. The fracture surface of the welded specimen showed brittle fracture compared with that in the BM. This finding was in good agreement with the lower elongation of the welded specimens in the tensile test (Figure 13).

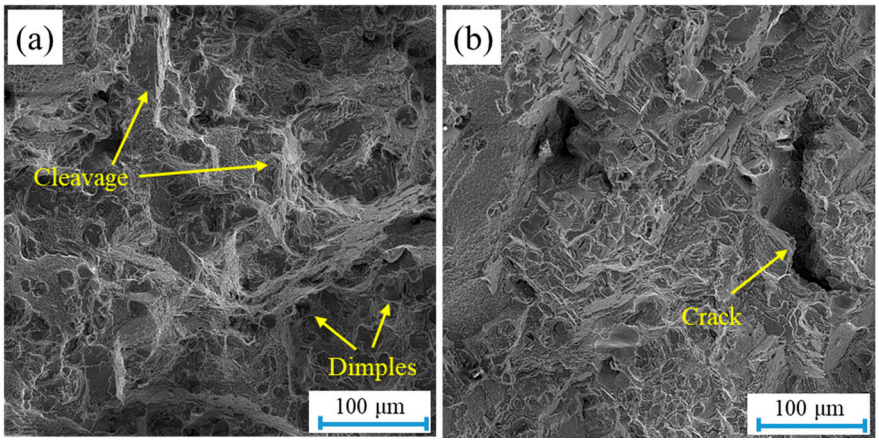


Figure 14. Fracture surface after tensile test: (**a**) BM and (**b**) A1 welded specimen.

3.3.2. Hardness Profile

Hardness was measured at the cross-sections of the welded specimens under different welding conditions. Figure 15 shows the variation in hardness in the three zones: BM, HAZ and FZ. The hardness decreased continuously from the BM to the FZ and increased clearly at the boundary between the FZ and HAZ. The volume fraction of γ' precipitates discretion might be responsible for this phenomenon [21]. The outcomes of the hardness tests and metallographic investigations indicated that the total length of welding-induced cracks could be increased dramatically with increasing hardness in the HAZ.

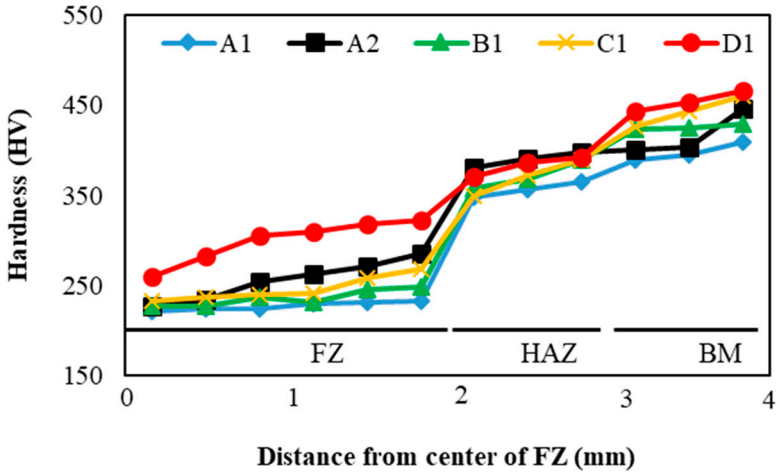


Figure 15. Changes in hardness profile in the welding zone.

4. Conclusions

The effects of pre-weld heat treatment and welding heat input on the microstructure, hot tensile behaviour and crack formation of IN-939 weldments were investigated. The following conclusions can be drawn:

1. Metallographic investigations indicated that the microstructures of IN-939 were highly susceptible to cracking during welding. The grain-boundary type cracks were initiated from the boundary between the weld metal and HAZ and mostly were propagated into the base metal. Many re-melting zones existed in the vicinity of the cracks, which were directly formed from the reaction between intergranular liquation and mechanical driving force due to tensile stresses created during welding.
2. The elemental analysis of the melted layer showed the existence of Ni, C, Cr and Co as well as the co-existence of $M_{23}C_6$ carbide and γ phase. This finding signified the formation of $M_{23}C_6$

carbides at the grain boundaries and γ′ precipitates around grain boundaries, which are the major causes of intergranular liquation.

3. Pre-weld heat treatment and welding heat input affected the microstructure and grain sizes of the HAZ. In all specimens, the volume fraction and average diameter of gamma-prime precipitates in the HAZ were affected by welding, resulting in a sharp decrease in hardness. The outcomes of the hardness tests and metallographic investigations indicated that the total length of welding-induced cracks increased with increasing HAZ hardness.
4. Tensile tests were performed on the base metal and welded specimens with the best properties. Welding did not affect the yield strength of the superalloy but reduced the ultimate strength and elongation by as much as 92% and 50%, respectively, of those of the BM within 600 °C–800 °C.
5. The increase in temperature decreased the hot tensile, yield and ultimate strengths of the base metal and welded specimen. However, the lowest tensile elongation was observed at 700 °C.

Author Contributions: Conceptualization, A.M. and H.O.; formal analysis, A.M., H.O. and Z.S.; investigation, A.M., H.O., Z.S. and C.H.G.; methodology, A.M. and H.O.; project administration, H.O. and Z.S.; supervision, H.O., Z.S. and C.H.G.; visualization, Z.S. and A.H.B.; writing—original draft, A.M.; writing—review and editing, H.O., Z.S. and A.H.B. All authors have read and agreed to the published version of the manuscript.

Funding: This research was partially funded by Universiti Kebangsaan Malaysia, grant number MI-2019-025.

Conflicts of Interest: The authors declare no conflict of interest.

References

1. Chang, B.; Yang, S.; Liu, G.; Li, W.; Du, D.; Ma, N. Influences of Cooling Conditions on the Liquation Cracking in Laser Metal Deposition of a Directionally Solidified Superalloy. *Metals* **2020**, *10*, 466. [CrossRef]
2. Diaz-Álvarez, A.; Miguélez, H.; Cantero, J.L. Finishing turning of Ni superalloy haynes 282. *Metals* **2018**, *8*, 843. [CrossRef]
3. Doroudi, A.; Shamsipur, A.; Omidvar, H.; Vatanara, M. Effect of transient liquid phase bonding time on the microstructure, isothermal solidification completion and the mechanical properties during bonding of Inconel 625 superalloy using Cr-Si-B-Ni filler metal. *J. Manuf. Process.* **2019**, *38*, 235–243. [CrossRef]
4. Nowak, W.J.; Ochał, K.; Wierzba, P.; Gancarczyk, K.; Wierzba, B. Effect of substrate roughness on oxidation resistance of an aluminized ni-base superalloy. *Metals* **2019**, *9*, 782. [CrossRef]
5. Bapokutty, O.; Sajuri, Z.; Syarif, J.; Said, A.R. Fracture Behavior of Inconel 718 at High Temperature. In *Key Engineering Materials*; Trans Tech Publications Ltd.: Stafa-Zurich, Switzerland, 2011; Volume 462, pp. 1244–1249.
6. Doroudi, A.; Pilehrood, A.E.; Mohebinia, M.; Dastgheib, A.; Rajabi, A.; Omidvar, H. Effect of the isothermal solidification completion on the mechanical properties of Inconel 625 transient liquid phase bond by changing bonding temperature. *J. Mater. Res. Technol.* **2020**, *9*, 10355–10365. [CrossRef]
7. Zhao, J.-R.; Hung, F.-Y.; Lui, T.-S. Erosion Resistance and Particle Erosion-Induced Tensile Embrittlement of 3D-Selective Laser Melting Inconel 718 Superalloy. *Metals* **2020**, *10*, 21. [CrossRef]
8. Kangazian, J.; Shamanian, M. Electron Back Scattered Diffraction Study of Dissimilar Welding Between the Super Duplex Stainless Steel and the Ni - Based Superalloy. *Met. Mater. Int.* **2019**, *25*, 1287–1300. [CrossRef]
9. Chen, K.-C.; Chen, T.-C.; Shiue, R.-K.; Tsay, L.-W. Liquation cracking in the heat-affected zone of IN738 superalloy weld. *Metals* **2018**, *8*, 387. [CrossRef]
10. Ramkumar, K.D.; Sai, R.J.; Sridhar, G.; Reddy, V.S.; Prabaharan, P.; Arivazhagan, N.; Sivashanmugham, N. Influence of filler metals in the control of deleterious phases during the multi-pass welding of Inconel 718 plates. *Acta Metall. Sin. Engl. Lett.* **2015**, *28*, 196–207. [CrossRef]
11. Wang, T.F.; Di, X.J.; Li, C.N.; Wang, J.M.; Wang, D.P. Effect of δ Phase on Microstructure and Hardness of Heat-Affected Zone in TIG-Welded GH4169 Superalloy. *Acta Metall. Sin. Engl. Lett.* **2018**. [CrossRef]
12. Taheri, M.; Halvaee, A.; Farshid, S.; Bozorg, K. Effect of Pre- and Post-weld Heat Treatment on Microstructure and Mechanical Properties of GTD-111 Superalloy Welds. *Met. Mater. Int.* **2019**. [CrossRef]
13. Said, A.; Syarif, J.; Sajuri, Z. HAZ Characterization of GTD-111 Nickel based superalloy welding. *Int. J. Mater. Eng. Tech.* **2009**, *2*, 133–139.

14. Xie, J.; Ma, Y.; Xing, W.; Zhang, L.; Ou, M.; Liu, K. Heat-affected zone crack healing in IN939 repaired joints using hot isostatic pressing. *Weld. World* **2018**, *62*, 471–479. [CrossRef]
15. Bidron, G.; Doghri, A.; Malot, T.; Fournier-dit-chabert, F.; Thomas, M.; Peyre, P. Reduction of the hot cracking sensitivity of CM-247LC superalloy processed by laser cladding using induction preheating. *J. Mater. Process. Tech.* **2020**, *277*, 116461. [CrossRef]
16. Sidhu, R.K.; Ojo, O.A.; Chaturvedi, M.C. Microstructural analysis of laser-beam-welded directionally solidified INCONEL 738. *Metall. Mater. Trans. A* **2007**, *38*, 858–870. [CrossRef]
17. Sajuri, Z.; Said, A.R.; Ibrahim, M.L.; Syarif, J. Premature Failure of Gas Turbine Blade. In *Key Engineering Materials*; Trans Tech Publications Ltd.: Stafa-Zurich, Switzerland, 2011; Volume 462, pp. 325–330.
18. Ye, X.; Zhang, P.; Zhao, J.; Ma, P. E ff ect of macro- and micro-segregation on hot cracking of Inconel 718 superalloy argon-arc multilayer cladding. *J. Mater. Process. Tech.* **2018**, *258*, 251–258. [CrossRef]
19. Ola, O.T.; Ojo, O.A.; Chaturvedi, M.C. Role of filler alloy composition on laser arc hybrid weldability of nickel-base IN738 superalloy. *Mater. Sci. Technol.* **2014**, *30*, 1461–1469. [CrossRef]
20. Tajally, M. Effects of Filler Metals on Heat-Affected Zone Cracking in IN-939 Superalloy Gas-Tungsten-Arc Welds. *J. Mater. Eng. Perform.* **2020**, *29*, 1068–1079. [CrossRef]
21. González, M.A.; Martínez, D.I.; Pérez, A.; Guajardo, H.; Garza, A. Microstructural response to heat affected zone cracking of prewelding heat-treated Inconel 939 superalloy. *Mater. Charact.* **2011**, *62*, 1116–1123. [CrossRef]
22. Albarrán, M.A.G.; Martínez, D.I.; Díaz, E.; Díaz, J.C.; Guzman, I.; Saucedo, E.; Guzman, A.M. Effect of preweld heat treatment on the microstructure of heat-affected zone (HAZ) and weldability of Inconel 939 superalloy. *J. Mater. Eng. Perform.* **2014**, *23*, 1125–1130. [CrossRef]
23. Kazempour-Liasi, H.; Tajally, M.; Abdollah-Pour, H. Effects of pre-and post-weld heat treatment cycles on the liquation and strain-age cracking of IN939 superalloy. *Eng. Res. Express* **2019**, *1*, 25026. [CrossRef]
24. Arhami, F.; Mirsalehi, S.E. The effect of heat treatment sequence on microstructure and mechanical properties of diffusion brazed IN-939 superalloy. *J. Mater. Process. Technol.* **2019**, *266*, 351–362. [CrossRef]
25. Marchese, G.; Bassini, E.; Aversa, A.; Lombardi, M.; Ugues, D.; Fino, P.; Biamino, S. Microstructural evolution of post-processed hastelloy X alloy fabricated by laser powder bed fusion. *Materials* **2019**, *12*, 486. [CrossRef] [PubMed]
26. Raza, T.; Hurtig, K.; Asala, G.; Andersson, J.; Svensson, L.-E.; Ojo, O.A. Influence of heat treatments on heat affected zone cracking of gas tungsten arc welded additive manufactured alloy 718. *Metals* **2019**, *9*, 881. [CrossRef]
27. Yin, H.; Gao, Y.; Gu, Y. Effects of post-welding heat treatment on microstructure and mechanical properties of welding joint of new Ni-Fe based superalloy with Haynes 282 filler metal. *Mater. Sci. Eng. A* **2017**, *708*, 118–128. [CrossRef]
28. Hu, R.; Bai, G.; Li, J.; Zhang, J.; Zhang, T.; Fu, H. Precipitation behavior of grain boundary M23C6 and its effect on tensile properties of Ni–Cr–W based superalloy. *Mater. Sci. Eng. A* **2012**, *548*, 83–88. [CrossRef]
29. Gong, L.; Chen, B.; Du, Z.; Zhang, M.; Liu, R.; Liu, K. Investigation of Solidification and Segregation Characteristics of Cast Ni-Base superalloy K417G. *J. Mater. Sci. Technol.* **2018**, *34*, 541–550. [CrossRef]
30. Jahangiri, M.R.; Arabi, H.; Boutorabi, S.M.A. Comparison of microstructural stability of IN939 superalloy with two different manufacturing routes during long-time aging. *Trans. Nonferr. Met. Soc. China* **2014**, *24*, 1717–1729. [CrossRef]
31. Kuo, C.; Yang, Y.; Bor, H.; Wei, C.; Tai, C. Aging effects on the microstructure and creep behavior of Inconel 718 superalloy. *Mater. Sci. Eng. A* **2009**, *511*, 289–294. [CrossRef]
32. Liu, L.R.; Jin, T.; Zhao, N.R.; Sun, X.F.; Guan, H.R.; Hu, Z.Q. Formation of carbides and their effects on stress rupture of a Ni-base single crystal superalloy. *Mater. Sci. Eng. A* **2003**, *361*, 191–197. [CrossRef]
33. Li, X.; Wang, L.; Yao, X.L.; Dong, W.J. Effect of Aging Heat Treatment on the Microstructure and Creep Properties of the Cast Ni-Based Superalloy at Low Temperature. *Acta Metall. Sin. Engl. Lett.* **2018**, *32*, 651–658. [CrossRef]
34. Lvov, G.; Levit, V.I.; Kaufman, M.J. Mechanism of primary MC carbide decomposition in Ni-base superalloys. *Metall. Mater. Trans. A* **2004**, *35*, 1669–1679. [CrossRef]
35. Tan, Y.G.; Liu, F.; Wen, A.; Wei, D.; Xiao, H.; Yao, Y.; Zhang, W.W.; Sun, W.R. Element Segregation and Solidification Behavior of a Nb, Ti, Al Co - Strengthened Superalloy ЭK151. *Acta Metall. Sinica (English Lett.)* **2019**. [CrossRef]

36. Huang, Y.; Lei, W.; Yang, L.I.U.; Fu, S.-M.; Wu, J.-T.; Ping, Y.A.N. Microstructure evolution of a new directionally solidified Ni-based superalloy after long-term aging at 950° C upto 1000 h. *Trans. Nonferr. Met. Soc. China* **2011**, *21*, 2199–2204. [CrossRef]
37. Bai, G.; Li, J.; Hu, R.; Tang, Z.; Xue, X.; Fu, H. Effect of temperature on tensile behavior of Ni–Cr–W based superalloy. *Mater. Sci. Eng. A* **2011**, *528*, 1974–1978. [CrossRef]
38. Kazempour-Liasi, H.; Tajally, M.; Abdollah-Pour, H. A Study on Microstructure and Phase Transformation in the Weld Fusion Zone of TIG-Welded IN939 with IN625 and IN718 as Filler Metal. *Metall. Mater. Trans. A* **2020**, *51*, 2163–2179. [CrossRef]
39. Lachowicz, M.; Dudziński, W.; Podrez-Radziszewska, M. TEM observation of the heat-affected zone in electron beam welded superalloy Inconel 713C. *Mater. Charact.* **2008**, *59*, 560–566. [CrossRef]
40. Danis, Y.; Arvieu, C.; Lacoste, E.; Larrouy, T.; Quenisset, J.M. An investigation on thermal, metallurgical and mechanical states in weld cracking of Inconel 738LC superalloy. *Mater. Des.* **2010**, *31*, 402–416. [CrossRef]
41. Yan, F.; Liu, S.; Hu, C.; Wang, C.; Hu, X. Liquation cracking behavior and control in the heat affected zone of GH909 alloy during Nd: YAG laser welding. *J. Mater. Process. Technol.* **2017**, *244*, 44–50. [CrossRef]
42. Li, S.; Li, K.; Cai, Z.; Pan, J. Behavior of M23C6 phase in Inconel 617B superalloy during welding. *J. Mater. Process. Technol.* **2018**, *258*, 38–46. [CrossRef]
43. Pilehrood, A.E.; Omidvar, H.; Shamsipur, A.; Sajuri, Z. Influence of transient liquid phase bonding followed by homogenization on the fatigue lifetimes of inconel 738 at elevated temperature. *J. Manuf. Process.* **2020**, *55*, 348–358. [CrossRef]
44. Sajjadi, S.A.; Nategh, S.; Isac, M.; Zebarjad, S.M. Tensile deformation mechanisms at different temperatures in the Ni-base superalloy GTD-111. *J. Mater. Process. Technol.* **2004**, *155*, 1900–1904. [CrossRef]
45. Pilehrood, A.E.; Omidvar, H.; Shamsipur, A.; Khakian-Ghomi, M. Effect of transient liquid phase bonding followed by homogenization on the microstructure and hot tensile behavior of Inconel 738 superalloy. *J. Manuf. Process.* **2019**, *48*, 110–118. [CrossRef]
46. Shi, Z.; Liu, S.; Yu, J.; Li, J. Tensile Behavior of the Second Generation Single Crystal Superalloy DD6. *J. Iron Steel Res. Int.* **2015**, *22*, 738–742. [CrossRef]

Publisher's Note: MDPI stays neutral with regard to jurisdictional claims in published maps and institutional affiliations.

© 2020 by the authors. Licensee MDPI, Basel, Switzerland. This article is an open access article distributed under the terms and conditions of the Creative Commons Attribution (CC BY) license (http://creativecommons.org/licenses/by/4.0/).